RSC Advances

ROYAL SOCIETY OF CHEMISTRY

PAPER

View Article Online
View Journal | View Issue

Check for updates

Cite this: *RSC Adv.*, 2025, **15**, 26552

Tuning ZnO photocatalysts *via* C and Ce Co-doping: a comparative approach using hydrothermal and microwave synthesis†

Thi Viet Ha Luu, *[a] Thi Lieu Nguyen,[a] Thi My Hien Bach,[a] Nguyen Trung Dung, [b] Nguyen Nhat Huy [cd] and Huu Phuc Dang *[e]

Received 19th May 2025
Accepted 15th July 2025

DOI: 10.1039/d5ra03520a

rsc.li/rsc-advances

In this study, C- and Ce-doped ZnO materials were synthesized by two methods: hydrothermal method (CCZ-HT) and microwave method (CCZ-MA), both using the same starting materials. The different heating stages of the methods produce distinct morphologies, doping concentrations, and some other characteristics. CCZ-HT consists of nanoellipsoids, while CCZ-MA consists of nanoflakes. The doping concentrations of cerium and carbon in CCZ-MA are higher than those in CCZ-HT. The types of crystal defects in the doped materials are different, leading to differences in their absorption and emission properties. The band gap energy of CCZ-MA is 2.85 eV, which is lower than that of CCZ-HT (2.92 eV). While CCZ-HT does not exhibit near-infrared emissions, CCZ-MA exhibits relatively strong emissions. CCZ-HT and CCZ-MA had a degradation capacity for ofloxacin (Ofx) under visible light that was 2.63 and 3.38 times superior to that of pure ZnO, respectively. The addition of Ce and C improved the band structure by slightly moving the conduction band and reducing the band gap, which allowed for better light absorption in the visible range and helped separate charge carriers. These enhancements immediately facilitated enhanced photocatalytic efficacy in the breakdown of ofloxacin. The CCZ-MA material exhibited superior photocatalytic activity due to its advantageous shape, increased surface area, and enhanced charge trapping capability associated with flaws. The functions of photo oxidized fragments and reaction intermediates were also examined. This study postulated a photodegradation mechanism for Ofx.

1. Introduction

Currently, the problem of antibiotic residues in the aquatic environment due to wastewater from the pharmaceutical industry, hospitals, and human and animal excretions is of great concern.[1] Long-term accumulation of antibiotics in the environment can aggravate the emergence and spread of antibiotic-resistant bacteria (ARB) and genes (ARG).[2] The antibiotic ofloxacin (OFX) belongs to the fluoroquinolone family and is one of the most widely consumed antibiotics for animal husbandry and human use. Due to the presence of fluorine in its molecules, ofloxacin is effective, stable, and can effectively break down bacteria. The harmful effects of ofloxacin residues are well known, including stopping plants from growing, lowering the variety of bacteria, disrupting the natural balance of elements, and negatively affecting human health through the food chain.[2] Additionally, OFL can alter the structure and interactions of bacteria by lowering nitrogen fixation, photosynthesis, and metabolism.[3] OFX has been detected in surface water near pharmaceutical plants at 85 to 41 μg L^{-1} and in treated hospital wastewater at 0.8 to 19.8 μg L^{-1}.[4,5] Therefore, treating OFX in polluted water sources before discharging it into the environment is a practical issue.

Reports have shown that the advanced oxidation process (AOP), which uses photocatalysis, is an effective method for removing antibiotic pollutants from water.[6–12] In recent decades, scientists have extensively investigated photocatalysis using ZnO, finding it a compelling subject with significant research interest. ZnO has important physical and chemical properties, such as being a semiconductor with a wide band gap of about 3.3 eV, a strong exciton binding energy of around 60

---

[a] *Faculty of Chemical Engineering, Industrial University of Ho Chi Minh City, 12 Nguyen Van Bao, Hanh Thong Ward, Ho Chi Minh City, 700000, Vietnam. E-mail: luuthivietha@iuh.edu.vn*

[b] *Faculty of Physics and Chemical Engineering, Le Quy Don Technical University, 236 Hoang Quoc Viet St., Nghia Do Ward, Hanoi, Vietnam*

[c] *Faculty of Environment and Natural Resources, Ho Chi Minh City University of Technology (HCMUT), 268 Ly Thuong Kiet St., Dien Hong Ward, Ho Chi Minh City, Vietnam*

[d] *Vietnam National University Ho Chi Minh City, Vo Truong Toan St., Linh Xuan Ward, Ho Chi Minh City, Vietnam*

[e] *Faculty of Fundamental Science, Industrial University of Ho Chi Minh City, 12 Nguyen Van Bao, Hanh Thong Ward, Ho Chi Minh City, 700000, Vietnam. E-mail: danghuuphuc@iuh.edu.vn*

† Electronic supplementary information (ESI) available. See DOI: **https://doi.org/10.1039/d5ra03520a**

meV, and an excellent ability to absorb UV and sunlight. Additionally, ZnO is very stable in both chemical and optical terms, reacts well over a wide range of pH levels, is environmentally safe, and affordable.[13,14] Although ZnO has many outstanding qualities, it has some drawbacks, such as a large band gap (3.3 eV), which limits its excellent photocatalytic activity to ultraviolet light. The rapid recombination of electrons and holes in ZnO reduces its effectiveness.[15–17] This has limited the effective use of ZnO as a powerful photocatalyst under visible light and sunlight.

Physical modifications, electronic structures, and surface morphology of ZnO can overcome its limitations. Material characteristics, such as crystallite size, band gap energy, and lattice defect concentration, influence these modifications. Doping, a process that introduces non-metallic, metallic, or co-doped metals and non-metals into the ZnO lattice, enables these modifications. Non-metallic doping usually adds extra energy levels in the space between the bands and just above the valence band of ZnO, which lowers the band gap and increases the range of light that can be absorbed into the visible light area.[18–22] Among non-metallic dopants, S, C, and N have been the most studied. Previous studies have indicated a significant increase in the bandgap energy and photocatalytic activity of ZnO under visible-light irradiation.[23,24] Weilai Yu *et al.* studied the electronic structure, light properties, and effective masses of charge carriers using DFT density functional theory calculations to make comparisons. The results showed that N- and C-doped ZnO exhibited much stronger light absorption in both the visible and ultraviolet regions than S-doped ZnO. This was explained by the idea that N- and C-doping can create empty spots in the material that help lower the energy needed for electrons to move, making it easier for light to be absorbed by the material. In comparison, S-doped ZnO had very few vacancies, which led to only a slight increase in light absorption, and its improved photocatalytic performance was probably due to the reduction in the band gap being smaller. C doping is considered the best way to reduce the recombination of excited charges compared to N and S doping, which improves the quantum efficiency of ZnO-based photocatalysts.[25] Furthermore, compared with N and S doping, C doping is considered more environmentally friendly because of its minimal impact on secondary reaction products throughout the process.

Cerium, the most prevalent rare earth element in nature, has garnered significant interest because of its unique properties. Cerium has an empty 4f shell and can exist in different forms (Ce^{4+}/Ce^{3+}). Therefore, when electrons shift between the 5d and 4f states or from Ce^{3+} to Ce^{4+}, the electrical and optical properties of the material can be significantly altered.[26,27] Studies have shown that adding cerium creates spaces for oxygen, and cerium ions can capture electrons, which helps prevent the rapid recombination of electron–hole pairs.[28,29] The fabrication method significantly influences the structural, morphological, optical, electrical, and photocatalytic properties of the materials. Hydrothermal synthesis has been regarded as an effective technique for regulating the morphology and dimensions of materials. Hydrothermal products frequently exhibit elevated crystallization and purity at lower synthesis temperatures than those of alternative methods. Nevertheless, it has limitations, including the need for specific pressure and temperature conditions, which render the experimental configuration relatively complex and time-intensive and constrain the capacity for large-scale production. Microwave-assisted chemical synthesis is advantageous because of the rapid and uniform heating of the entire reaction system, elevated reaction rates, and enhanced selectivity. The water in the reaction solution acts as a dipole solvent, where heat is generated by the movement and interaction of water molecules that are affected by a rapidly changing electric field. The ions in the solution continuously move because of the changing electric field, which quickly raises the local temperature due to friction and collisions, allowing the solution to swiftly become supersaturated and form crystals.[30] Consequently, this method is a more efficient synthesis technique in terms of energy and time compared to traditional heating methods.

In the preceding investigation, hydrothermal synthesis was employed to fabricate ZnO materials co-doped with carbon and cerium, referred to as CCZ-HT.[31] The investigation encompassed many physicochemical parameters, including structure (XRD), morphology (SEM), bond vibration characteristics (FT-IR), optical properties (UV-vis-DRS), surface chemistry (EDS), and photocatalytic activity for the destruction of methylene blue. This study involved the synthesis of ZnO materials co-doped with C and Ce by hydrothermal (CCZ-HT) and microwave (CCZ-MA) processes, utilising the same precursor materials as the prior research. The photocatalytic characteristics of CCZ-HT and CCZ-MA materials have been extensively explored and analysed in detail. This study further examined the characteristics of structural defects (PL), surface chemistry and binding energy (XPS), specific surface area (BET), electrochemical properties (Mott–Schottky), and photocatalytic activity for the degradation of Ofx, in addition to the typical physicochemical properties analysed and discussed in the previous study. The findings presented in each analysis provide a comparison between the two materials: CCZ-HT and CCZ-MA. Moreover, HPLC-MS analyses were performed to identify the products generated during the intermediate phase, and studies were undertaken to elucidate the role of reactive species in the degradation of organic matter (Ofx). This established the foundation for proposing the reaction mechanism for the degradation of Ofx in the catalyst.

2. Materials and methods

2.1. Chemical reagents

All the reagents used in this study were of analytical grade and obtained without further purification. $Zn(CH_3COO)_2\ 2H_2O$, $Ce(NO_3)_3 \cdot 6H_2O$, C_2H_5OH, NaOH, were bought from the Hemedia–India. Poly(-vinyl alcohol) (PVA, $M = 145\,000$ g mol, 99%), $AgNO_3$ (99.9%), ethylenediamine tetraacetic acid (EDTA, >99%), and isopropanol (Isop, 99.5%), and 1,4-benzoquinone (*p*-BQ, 98%) were purchased from Merck (USA). Ofloxacin (Ofx) was supplied by Macklin (China).

2.2. Synthesis of C, Ce-codoped ZnO (CCZ-HT and CCZ-MA)

2.2.1 Synthesis of CCZ-HT. C, Ce-codoped ZnO nano elipsoids were prepared according to previously report by hydrothermal method with zinc acetate, cerium nitrate, ethanol solvent, and sodium hydroxide precursors.[31] The molar ratio of Ce^{3+}/Zn^{2+} was 3.0%, and of PVA/Zn^{2+} was 15%. Briefly, 0.662 g $Zn(CH_3COO)_2 \cdot 2H_2O$ and 0.040 g $Ce(NO_3)_3 \cdot 6H_2O$ were mixed in 70 mL absolute ethanol to form a clear solution. In another solution, 0.015 g of polyvinyl alcohol (PVA) was added to a beaker containing 30 mL of distilled water and stirred continuously using a magnetic stirrer to form an aqueous solution. The clear solutions were mixed and stirred for 1 h. Then, a solution of 1.2 g NaOH in 50 mL C_2H_5OH was added dropwise, and the mixture was stirred for 1 h. The resulting solution was transferred to a 200 mL Teflon-lined autoclave and heated in an oven at 150 °C for 20 h. The autoclave was cooled to room temperature, and the resulting product was separated by centrifugation, washed several times with distilled water and ethanol, and finally dried at 80 °C for 8–10 h. The sample is denoted as CCZ-HT.

2.2.2 Synthesis of CCZ-MA. The production of the CCZ-MA catalyst followed the same procedure as that of the CCZ-HT catalyst, except that the reaction mixture was heated by reflux for 1 h using a microwave at 400 W.

2.3. Characterization of the materials

The crystal structures of the catalysts were examined using a Cu-Kα wavelength ($\mu = 1.54060$ Å) X-ray diffraction (XRD) instrument (D8 Advance, Bruker, Germany). Thermogravimetric analysis (TGA) and differential thermal analysis (DTA) were performed using a Labsys Evo system (SETARAM, France). Morphological characterization was conducted using a field emission scanning electron microscope (FESEM) model JSM-T800 from Jeol, Japan. Qualitative elemental analysis was performed using energy-dispersive X-ray spectroscopy (JEOL-2300). The functional groups present in the catalyst were detected by Fourier-transform infrared (FT-IR) analysis using a PerkinElmer (USA) instrument. Uniform UV-visible diffuse reflectance spectra (UV-vis DRS) were acquired using a V670-Jasco spectrophotometer manufactured in Japan. Photoluminescence (PL) spectra were obtained using a Horiba FL3C-22 Fluorolog-3 instrument. The surface chemical state of the samples was inferred using a PHI X-ray optoelectronic device (PHI Quantera SXM, Japan). Nitrogen adsorption isotherms were conducted at −196 °C using Quantachrome Autosorb iQMP/XR equipment. The specific surface areas were computed using the BET method, and the pore size distributions were ascertained by the BJH method.

2.4. Photocatalytic activity tests

The photocatalytic activity of the synthesized catalysts was evaluated by ofloxacin (Ofx) degradation studies carried out at ambient temperature. A 150 W halogen lamp was used as the illumination source. Each standard experiment involved suspending 0.05 g of the photocatalyst in 100 mL of Ofx solution at a concentration of 20 mg L^{-1}. To achieve adsorption–desorption equilibrium, the suspension was stirred in the dark for 60 min. The mixture was then exposed to visible light for 150 min. A 3 mL aliquot of the solution was collected at 15-minute intervals and centrifuged to eliminate any residual photocatalysts in the reaction media. Three replicates of each experiment were conducted to determine the standard error. The concentration of Ofx was quantitatively measured using a UV-vis spectrophotometer (Agilent Cary 3500 UV-vis spectrophotometer). The calibration curve was employed to ascertain the Ofx concentration, with optical density measured at the peak wavelength of 288 nm, and Ofx concentrations varying from 0 to 30 mg L^{-1}.

Moreover, the Ofx photodegradation process was examined using a pseudo-first-order kinetic model that relies on the linear relationship between ln (C_t/C_0) and reaction time t (eqn (1)).

$$\ln(C_t/C_0) = \ln(A_t/A_0) = kt \tag{1}$$

Let k (min^{-1}) represent the reaction rate constant, and t (min) denote the duration of irradiation. At time t, the concentration of Ofx is denoted as C_t (mg L^{-1}), and C_0 (mg L^{-1}) represents the initial concentration of Ofx. The optical densities of Ofx at t = 0 and t min are denoted as A_0 and A_t, respectively.

To assess the individual contributions of various reactive species generated during the photo-oxidation process and their respective functions, several scavenging species ($AgNO_3$, Isop, AO, and *p*-BQ) were employed in quenching tests for e^-, $^{\bullet}OH$, h^+, and $^{\bullet}O_2^-$, *etc.* The intermediate compounds generated during the photodegradation of Ofx were detected using mass spectrometry-positive electrospray ionization (ESI^+) with a capillary voltage of 3.0 kV, source temperature of 150 °C, dissolving temperature of 400 °C, and mass-to-charge ratio (*m*/*z*) between 0 and 400.

3. Results and discussion

3.1. Material characterization

Concurrent thermogravimetric and differential thermal analysis (TG-DTA) curves were obtained to investigate the thermal breakdown of these materials. The findings are shown in Fig. 1. The TGA profile of CCZ-HT in Fig. 1A indicates that thermal degradation mostly occurs at temperatures below 100 °C. A mass loss of 2.018% was observed within the temperature range of 30–70 °C, suggesting the evaporation of surface-adsorbed ethanol and water molecules. This phenomenon was also observed in the DTA curve associated with the endothermic peak at 70 °C. At temperatures above 80 °C, there was no mass loss, and the thermogravimetric curve remained somewhat constant. These results demonstrate the stability of the hydrothermal product at temperatures exceeding 80 °C.

The thermal analysis diagram of CCZ-MA (Fig. 1B) indicates a significant mass reduction (44.146%) within the temperature range of 50–120 °C, which corresponds to a peak in endothermic behavior at 100 °C. The reduction in mass was caused by the evaporation of water vapor and ethanol that had been absorbed onto the substrate surface. Subsequently, across the

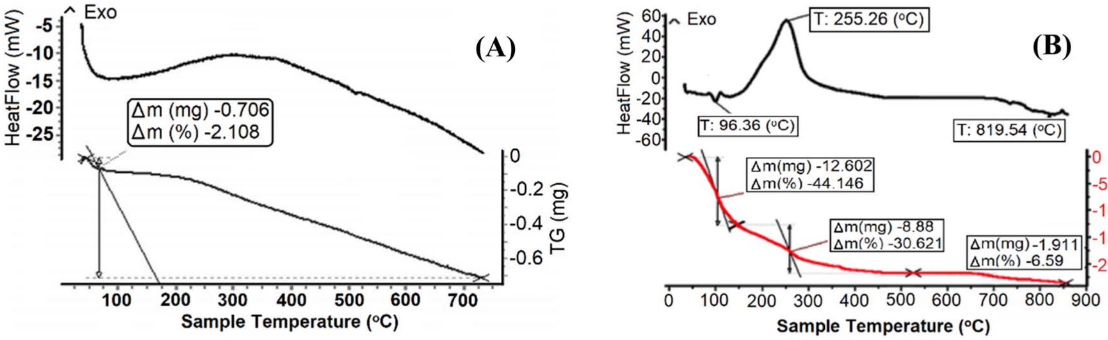

Fig. 1 TGA/DTG curves of CCZ-HT (A) and CCZ-MA (B).

temperature range of 120–430 °C, a measurable decrease in mass was detected on the TG curve, amounting to 30.621%. Additionally, an exothermic effect was observed in the DTA curve, characterized by a peak at 255.28 °C. The observed outcome is associated with the pyrolysis of hydroxide to oxide and the oxidation of organic components to carbon and CO_2. Ultimately, across the temperature range of 430–700 °C, the TG curve exhibited a nearly horizontal and steady pattern. Furthermore, no thermal impact was observed on the DTA curve. This suggests that the CCZ-MA product was generated in a crystalline state and remained stable in this temperature range.

The results of the DTA-TG analysis indicated that the CCZ-HT produced after hydrothermal treatment required drying at a temperature above 80 °C without further calcination. Meanwhile, the CCZ-MA produced by microwave-assisted circulation stirring required calcination at a temperature above 450 °C to obtain a pure catalyst.

The catalysts' crystal structure and phase composition were analysed using X-ray diffraction (XRD). Fig. 2A displays the X-ray diffraction (XRD) patterns of ZnO-HT, Ce-ZnO-HT, and CCZ-HT synthesised using the hydrothermal method, whereas Fig. 2B presents the X-ray diffraction (XRD) patterns of ZnO-MA, Ce-ZnO-MA, and CCZ-MA produced *via* microwave synthesis. The starting reaction mixtures employed were the same in both procedures.

Consistent with JCPDS standard 00-036-1451, all samples exhibit a hexagonal single-phase structure of ZnO with distinct diffraction peaks corresponding to lattice planes (100), (002), (101), (102), (110), (103), (200), (112), and (201).[32–34] Distinct diffraction peaks corresponding to the contaminants were not observed. Magnified images of the X-ray diffraction (XRD) patterns in the diffraction angle range of 30–38° are provided in Fig. 2A′ and 2B′ to clearly analyze the difference in diffraction peaks between the doped and pure samples. Fig. 2A′ and 2B′ demonstrate that the introduction of Ce^{3+} as a single dopant causes a light displacement of the diffraction peaks of ZnO towards a somewhat lower 2-theta angle and a wider diffraction angle breadth in comparison to pure ZnO. This observation suggests that Ce^{3+} successfully permeated the ZnO structure. The observed shift has been documented in our previous work[34,35] as well as in several other studies.[36–38] In the presence of co-doping of C and Ce, the diffraction peaks exhibited a minor shift towards a greater 2-theta angle. Additionally, the breadth of the diffraction peaks increased compared to that of undoped ZnO or Ce-doped ZnO. These findings suggest that ion ceries and C were introduced into the ZnO lattice. Co-doping of C and Ta into ZnO yielded comparable findings.[32] The broadening of the diffraction peak width resulted in a decrease in the crystal size. Hence, it can be inferred that the co-doping of carbon and cerium significantly decreased the size of the crystals and caused a slight positive shift in the diffraction peaks while leaving the crystal structure of ZnO unchanged.

Notably, the formation of various crystal lattice planes was observed for distinct synthesis processes. During hydrothermal synthesis, the crystals were gradually developed over an extended duration of 24 hours under conditions beyond the solvent's boiling point and at elevated autogenous pressure. Under these conditions, ZnO and Ce-doped ZnO crystals exhibited preferential growth on the (100) lattice plane, evidenced by the maximum intensity of the diffraction peak corresponding to the (100) lattice plane. Nonetheless, the CCZ-HT crystal formation mechanism exhibited preferential development on the (101) plane. This discrepancy may be attributable to the presence of PVA. PVA serves as a precursor for doping carbon with ethanol and functions as a surfactant that facilitates crystal formation along the (101) lattice plane. In contrast to hydrothermal synthesis, microwave synthesis, characterised by quick, intense, and uniform heating across the volume, facilitates powerful and effective collisions among reactant molecules. The microwave approach offers the benefit of rapid and uniform heating acceleration throughout the entire volume, resulting in the product being formed in a brief duration. Consequently, the ZnO-MA, Ce-ZnOMA, and CCZ-MA materials exhibited analogous lattice plane growth patterns, with the (101) lattice plane being more prominently developed, as indicated by the increased intensity of the diffraction peak. The CCZ materials synthesised using various processes exhibited unique morphologies and physicochemical features, which will be elaborated upon in the subsequent results.

Raman spectroscopy was employed to evaluate the structural integrity and defect states of the synthesized ZnO-based photocatalysts (Fig. 2C). The undoped ZnO sample exhibits distinct Raman peaks at ∼99, 333, 437, and 582 cm^{-1}, which correspond

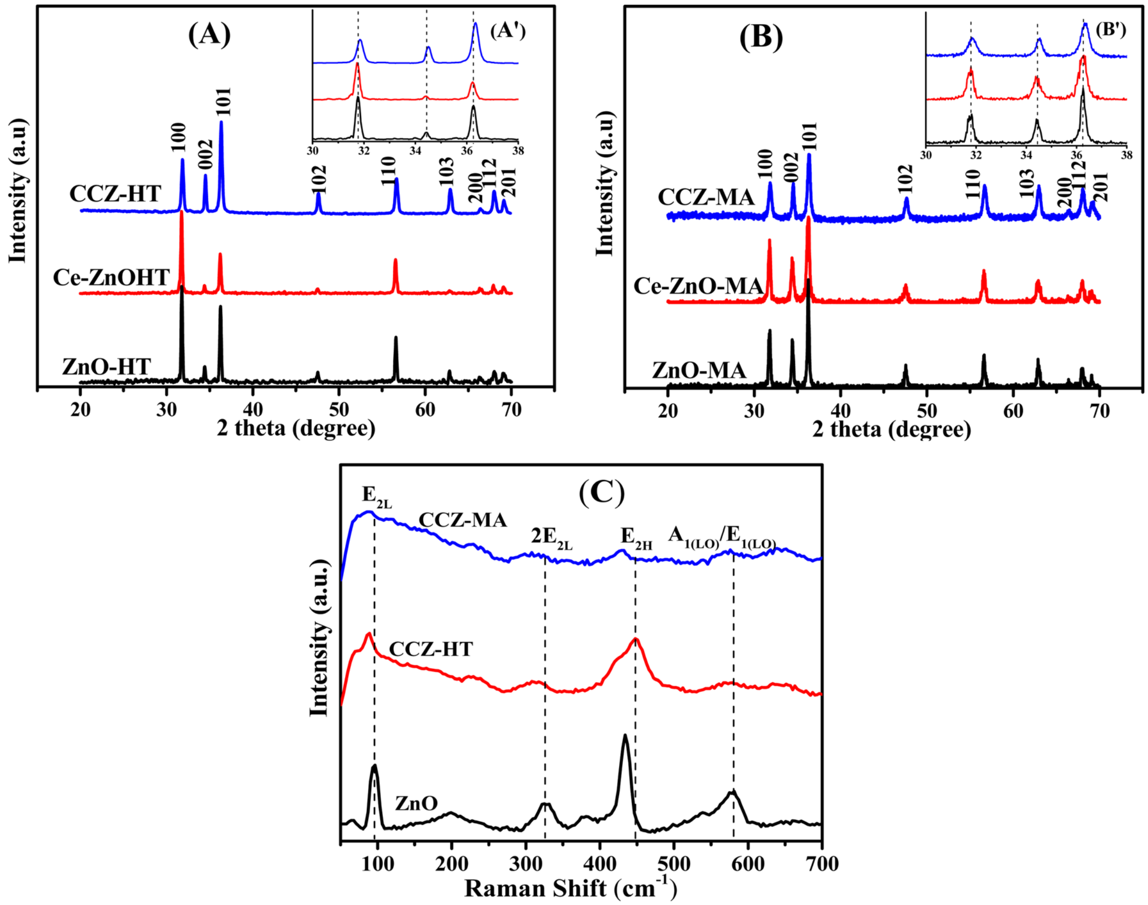

Fig. 2 XRD patterns of (A) ZnO-HT, Ce-ZnO-HT, and CCZ-HT synthesized using hydrothermal methods; (B) ZnO-MA, Ce-ZnO-MA, and CCZ-MA synthesized using microwave-assisted methods, and (C) Raman spectra of CCZ-MW, CCZ-HT, and ZnO.

to the E_{2L}, $2E_{2L}$, E_{2H}, and A_1(LO)/E_1(LO) vibrational modes of hexagonal wurtzite ZnO.[39,40] Among these, the sharp and intense E_{2H} mode at 437 cm^{-1} is characteristic of the long-range crystalline order of ZnO. In contrast, the CCZ-HT and CCZ-MW samples exhibited a marked broadening and reduction in the intensity of the E_{2H} peak, indicating increased lattice disorder resulting from Ce and C co-doping. Notably, the A_1(LO) mode around 582–585 cm^{-1} became more prominent in CCZ-MW, indicating a higher concentration of oxygen vacancies and defect states. These results are consistent with photoluminescence (PL) and X-ray photoelectron spectroscopy (XPS) analyses, confirming that microwave-assisted synthesis introduces more structural defects, which can serve as active sites for charge trapping and enhance the photocatalytic activity under visible light.

The variation in crystal growth under different synthesis conditions resulted in the formation of particles with varying morphologies. This process is illustrated in the FE-SEM images of the synthesized material (Fig. 3). The SEM image (Fig. 3B) shows that the CCZ-HT particles have a quasi-ellipsoidal shape and are nanosized. The hydrothermal synthesis was controlled at 150 °C within 20 h under a fairly high autogenous pressure. Nanoellipsoidal CCZ-HT particles with sharp, uniform shapes and no aggregation were formed. The one-step hydrothermal synthesis of CCZ-HT skips the calcination step, which prevents the particles from sticking together. In addition, the addition of PVA, which is a carbon source and acts as a surfactant, prevented the crystals from growing too long. Therefore, instead of forming rods like ZnO-HT (Fig. 3A), it led to the creation of nearly elliptical 0D CCZ-HT particles.

Fig. 3D shows that the CCZ-MA particles are thick flakes (flat particles) at the nanoscale, quite homogeneous, and the particles show slight aggregation. This aggregation may be due to the effect of the calcination process that occurred after microwave circulation. A previous study by Shen *et al.* found that the formation of ZnO flakes upon exposure to microwave radiation was due to the use of PVA as a surfactant. They suggested that PVA could inhibit the growth of the (001) lattice plane of ZnO, thereby preventing its expansion in that direction.[30,41] This inhibition resulted in the formation of ZnO flakes after 10 min of microwave heating. In this study, the microwave heating process was 1 h, which could have caused the aggregation of thin flakes into thicker ones, forming flat CCZ-MA particles. In contrast, the absence of PVA during the synthesis of ZnO-MA resulted in the material including mixed flake-like and rod-like structures (Fig. 3C).

The EDX spectra depicted in Fig. 3E and F verified the presence of four elements, specifically C, Ce, Zn, and O, in both

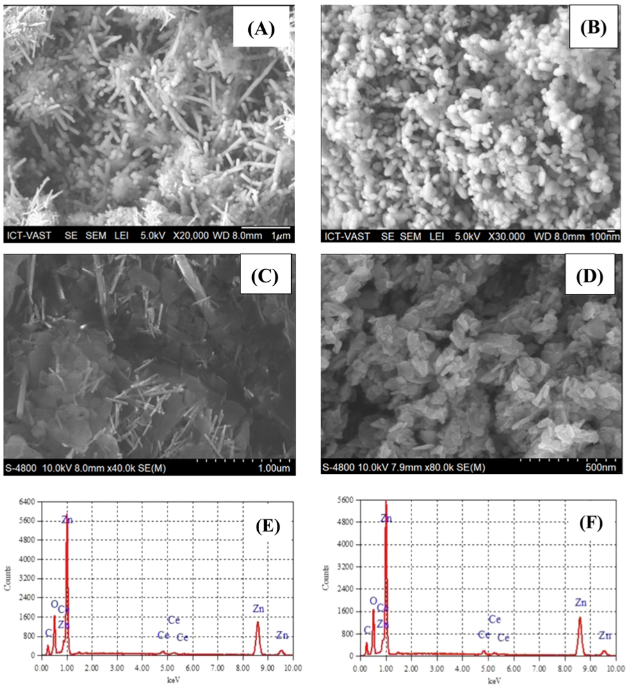

Fig. 3 FE-SEM images of (A) ZnO-HT, (B) CCZ-HT, (C) ZnO-MA, and (D) CCZ-MA; EDS spectra of (E) CCZ-HT and (F) CCZ-MA.

the CCZ-HT and CCZ-AM samples, without any other extraneous elements. The elemental composition analysis is shown in Table 1. The molar percentages of C (12.88%) and Ce (2.25%) doping in the CCZ-MA were higher than those in the CCZ-HT sample, which were (14.62%) and (2.02%), respectively. A trace quantity of Ce^{3+} salt precursor (3 mol%) was used as the donor for Ce doping. Under hydrothermal and microwave conditions, doped Ce can be introduced into the ZnO crystal lattice by partially replacing Zn^{2+} ions or by infiltrating crystal lattice defects. Furthermore, carbon can penetrate the crystal lattice of zinc oxide (ZnO) by partially replacing oxygen sites, entering oxygen vacancies, or existing at the material interface of ZnO. However, the source of the doped carbon is significant, as it is derived from acetate (CH_3COO^-) and PVA. Therefore, the mass ratio of the doped carbon was adapted according to the specific synthesis conditions. Rapid internal heating throughout the entire volume is caused by the mechanism and heat transmission properties of microwave radiation. Moreover, the collision and reaction rates demonstrate high velocity, enabling the entry of C into the ZnO lattice more easily than hydrothermal synthesis, which is marked by a slow and moderate reaction. Furthermore, microwave-assisted synthesis involves calcination, which serves to augment the chemical bonding properties of carbon inside the crystal lattice.

Table 1 Elemental composition of CCZ-HT and CCZ-MA samples

	CCZ-HT		CCZ-MA	
Element	Weight %	Atomic %	Weight %	Atomic %
O	8.39	24.99	8.48	24.89
Zn	82.45	60.11	81.07	58.23
Ce	5.92	2.02	6.71	2.25
C	3.24	12.88	3.74	14.62
Total	100.00	100.00	100.00	100.00

Infrared spectroscopy was employed to investigate the chemical bonding properties. The infrared spectra of the synthesized ZnO, CCZ-HT, and CCZ-MA are shown in Fig. 4A. The absorption peaks observed at around 3430 cm^{-1} and 1631 cm^{-1} correspond to the stretching and vibration of the O–H groups of surface adsorbed water.[42] The absorption peaks of CCZ-HT and CCZ-MA shifted toward higher wavenumbers compared to pure ZnO. The strong peaks with wavenumbers in the range of 420–610 cm^{-1} are characteristic of the vibrations of metal–oxygen bonds, including Zn–O and Ce–O–Zn.[35] The introduction of Ce led to a positive shift in the peaks of CCZ-HT (440 cm^{-1}) and CCZ-MA (428 cm^{-1}) compared to that of pure ZnO (422 cm^{-1}). These results validate the effective incorporation of Ce into the ZnO crystal lattice. Furthermore, the peaks at 865, 1380, 1442, and 1542 cm^{-1} confirm the presence of C doping in CCZ-HT and CCZ-MA.[38,43,44] More precisely, the peak observed at 865 cm^{-1} was attributed to the vibration of C–H bonds. The strong peaks at 1380 and 1442 cm^{-1} in the CCZ-MA material indicate the stretching of the C–O bond in the carboxylate group (COO^-). The weak absorption peak at 1542 cm^{-1} in the FTIR spectrum of CCZ-HT is attributed to the vibration of the C═O bond. The intensity of the absorption peak is related to the concentration of doped C. Consequently, it can be inferred that the concentration of doped carbon in the CCZ-MA sample was higher than that in the CCZ-HT sample. This result is consistent with the EDS analysis results. In addition, a modest absorption between 875 and 885 cm^{-1} is detected in the ZnO spectra, believed to be associated with the carbonate group.[45,46]

Fig. 4B presents the UV-vis-DRS spectra of CCZ-HT, CCZ-MA, Ce-ZnO, and ZnO samples, while Fig. 4C illustrates their corresponding Tauc plots. The doped samples exhibited much better optical absorption in both the UV and visible ranges than pure ZnO. Furthermore, the optical absorption edges of the doped materials exhibited a red shift compared to those of bare ZnO. The shift was minimal for the Ce-ZnO sample; however, it was pronounced for the CCZ-HT and CCZ-MA samples, respectively. The Tauc method estimated the band gap energies of CCZ-MA, CCZ-HT, Ce-ZnO, and ZnO to be 2.85, 2.92, 3.00, and 3.10 eV, respectively. It is known that doping metals (Fe, Ce) replace zinc sites and creates a local impurity state just below the conduction band of ZnO. In contrast, doping nonmetals (C, N) replaces oxygen sites and creates a local impurity state just above the valence band of ZnO.[47–49] This modulates the bandgap energy of ZnO and shifts the absorption threshold to the visible region. As a result, doping Ce alone reduces the band gap energy by 0.1 eV, while the simultaneous doping of C and Ce sharply reduces it from 0.18 to 0.25 eV. This evidence confirms the doping of C and Ce in the ZnO crystal lattice structure. Furthermore, the CCZ-MA samples had higher levels of Ce and C impurities than the CCZ-HT samples. However, they did not reach the critical concentration to become a charge recombination centre, which is why the CCZ-MA bandgap is smaller

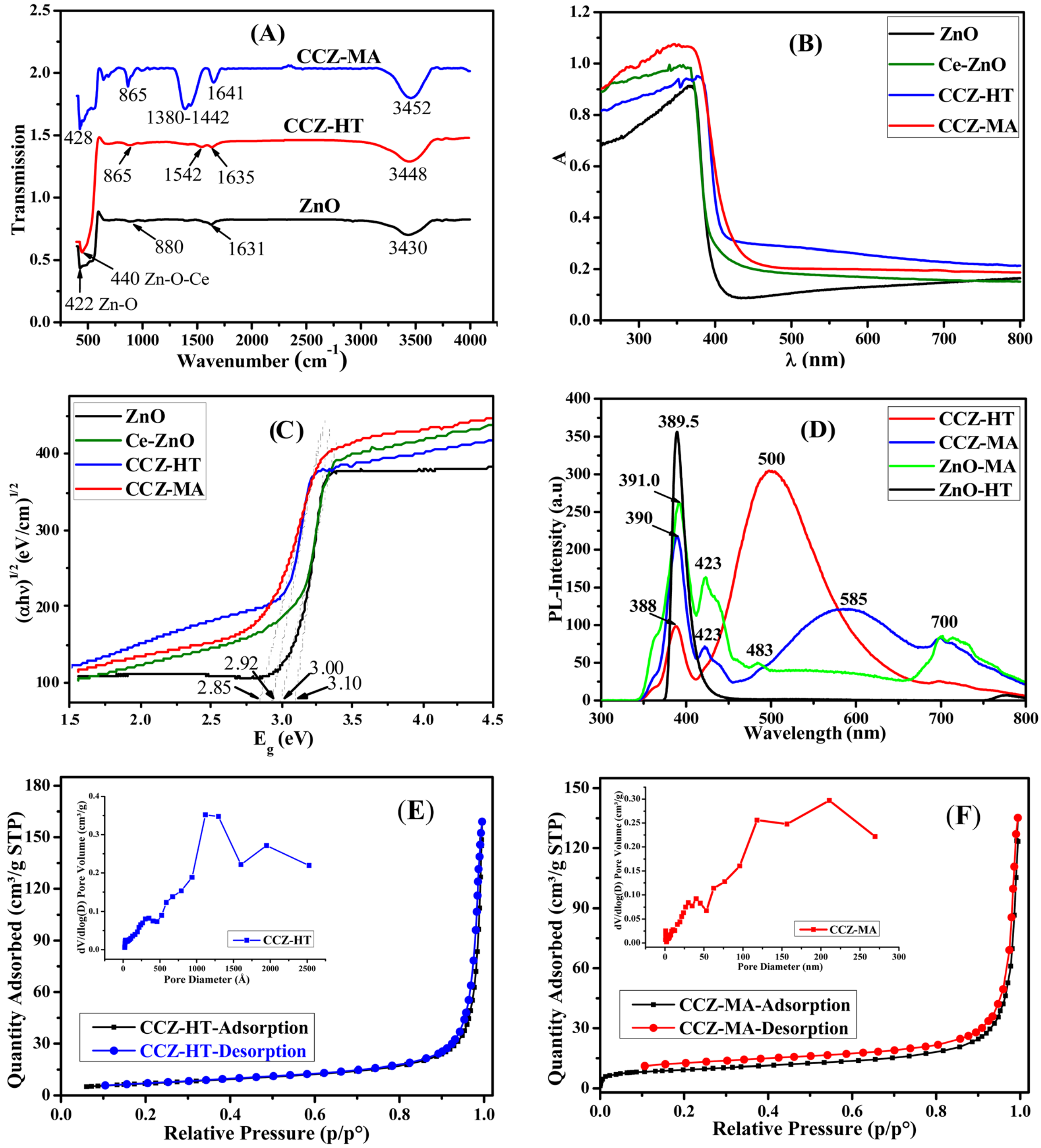

Fig. 4 (A) FT-IR spectra, (B) UV-vis diffuse reflectance spectra, (C) Tauc plots, (D) PL spectra, and (E), (F) the N_2 adsorption–desorption isotherms of synthesized samples.

than the CCZ-HT bandgap. In addition, the optical absorption edge characteristics of the co-doped materials were like those of pure ZnO, confirming the band structure remains direct. So, co-doping of C (3.24–3.74% by weight) and Ce (5.92–6.71 by weight) narrows the band gap and enhances the optical absorption but does not change the structure (XRD) or direct electron transfer properties of ZnO. For photocatalytic, optoelectronic, and solar cell applications, the direct electron transfer and superior light absorption of codoped ZnO materials are desirable.

The photoluminescence spectra of the synthesized samples (Fig. 4D) exhibited emission peaks in the near-UV, visible, and near-IR regions. The strong UV light emissions at approximately 390 nm are caused by excitons coming together near the band edge, which is typical for wurtzite ZnO. The UV emissions from CCZ-HT and CCZ-MA were weaker and occurred at lower energies than those from ZnO-HT and ZnO-MA, respectively. The intensity of these peaks diminished in the following order: ZnO-HT > ZnO-MA > CCZ-MA > CCZ-HT. The decrease in UV emission intensity shows that the doped ZnO is better at preventing the recombination of electron–hole pairs than pure ZnO. Of these, CCZ-HT demonstrated the most effective suppression. The visible emissions primarily correlate with the defect energy levels of the material, including zinc interstitials (Zn_i), extended zinc interstitials (ex-Zn_i), zinc vacancies (V_{Zn}), oxygen interstitials (O_i), and oxygen vacancies (V_O) defects. The weak, narrow, blue-violet emission at 423 nm for ZnO-MA and CCZ-MA is ascribed to the electron transition from the zinc vacancy level (V_{Zn}) to the valence band (VB) and from the shallow donor level of the zinc vacancies to the VB.[50,51] The pronounced and extensive visible emissions of CCZ-HT and CCZ-MA are noteworthy. The blue-green emission at 500 nm of CCZ-HT is primarily linked to the oxygen vacancy defect (V_O), whereas the yellow emission at 580 nm of CCZ-MA is attributed to the oxygen vacancy defect (V_O), interstitial oxygen (O_i), and zinc vacancy (Zn_i).[51] Visible emissions were only faintly observed in the ZnO-MA sample (peak at 483 nm) and were not detected in the ZnO-HT sample. Moreover, pronounced red and near-infrared (660–800 nm) emissions were distinctly detected in the microwave-synthesized samples, whereas only faint emissions were noted in the hydrothermally synthesized samples. The emissions were attributed to electron transfer from the deep donor to the acceptor center (DA mechanism) and correlated with the quantity of oxygen defects in the sample.[52] Additionally, Biroju *et al.* suggested that the NIR emissions originated from natural flaws in the ZnO nanorods.[53] The PL results of this study support this idea, showing that the strength and spread of the red and NIR emissions from ZnO-MA and CCZ-MA were almost the same. The near-infrared emission properties of CCZ-MA are important for photocatalytic applications that rely on solar energy.

Fig. 4E and F show the N_2 adsorption and desorption patterns, along with the pore size distributions for the CCZ-HT and CCZ-MA samples. The N_2 adsorption/desorption isotherms for both materials are identified as type IV, showing clear hysteresis loops. The H3 hysteresis loop shows that there is unlimited adsorption at high relative pressures (P/P^o), indicating slit-shaped pores in the structure.[54,55] The H3 hysteresis loop for the CCZ-HT sample appears at relative pressures (P/P^o) from 0.85 to 1.0, which can suggest the presence of macropores in the nanoellipsoids, while for the CCZ-MA sample it is seen between 0.1 and 1.0, indicating the existence of macropores and micropores in the nanoflakes.[56] The measured BET specific surface areas are 25.69 for CCZ-HT and 31.67 $m^2 g^{-1}$ for CCZ-MA. The BJH average pore diameter was ascertained to be approximately 35 nm for CCZ-HT and 17.9 nm for CCZ-MA.

These results are attributable to the surface shape, dopant concentration, and defect concentration inside the material's crystal lattice.

The oxidation states of the elements on the surfaces of the studied materials were examined using X-ray photoelectron spectroscopy (XPS). Gaussian deconvolution of each XPS spectrum was performed using XPS peak 4.1 software to obtain detailed compositional information of the samples. Fig. 5A, C, E and G show that the main peaks match the specific energy levels of the Zn 2p, O 1s, C 1s, and Ce 3d orbitals linked by spin–orbit coupling. The dominant Zn 2p peaks observed at 1021.38 eV and 1044.38 eV (Fig. 5A) represent the binding energies of the Zn $2p_{3/2}$ and Zn $2p_{1/2}$ spin–orbit components, respectively.[57] Deconvolution of the Zn $2p_{3/2}$ spectrum (Fig. 5B) revealed three distinct components at 1019.3, 1021.08, and 1022.6 eV. The peaks at 1021.08 eV and 1022.6 eV were observed in both materials, corresponding to Zn–O–C coordination and Zn–O_{vac} (V_O), respectively. The 1019.3 eV peak was only found in the CCZ-MA material, providing clear evidence that a Zn–C bond was formed in this composite system.[58,59]

The O 1s orbital (Fig. 5C) shows a large main peak at approximately 530 eV, which is divided into three smaller peaks (Fig. 5D) that correspond to the binding energies of Zn–O (529.6 eV), Zn–O–C or Zn–O_{vac} (530.5 eV), and C–O or C=O (532.05 eV), respectively.[60]

In addition, the XPS C 1s is split into peaks at 284.5, 285.86, and 288.38 eV (Fig. 5E and F), which are characteristic of the C–C (C=C), Zn–O–C, and C–O (C=O) binding energies, respectively.[61] The presence of Zn–O–C bonds in both the CCZ-MA and CCZ-HT samples demonstrated the doping of C into ZnO. Notably, for the CCZ-MA sample, C doping into ZnO was also demonstrated by Zn–C bonds. The presence of the Zn–O–C bond is a result of C doping, in which C^{4+} ions may have penetrated the zinc interstitial sites or partially replaced the Zn^{2+} ions. Meanwhile, the Zn–C bond demonstrates C doping into ZnO with the partial substitution of O^{2-} by C^{4-} or by penetration into oxygen vacancy defects.[62] The substitution of O^{2-} by C^{4-} ions is much more difficult than the substitution of Zn^{2+} by C^{4+} because the radius difference between O^{2-} (126 pm) and C^{4-} (260 pm) ions is much larger than that between Zn^{2+} (74 pm) and C^{4+} (30 pm). This can occur under vigorous synthesis conditions, such as those used in microwave synthesis. The evidence indicates that Zn–C bonds are present only in the CCZ-MA sample. Compared with microwave synthesis, hydrothermal synthesis is quite mild; perhaps because of this, C doping favors the replacement of oxygen ion sites or penetration into the oxygen vacancies. In addition, Jailes J. Beltrán[63] showed that, with a C doping concentration of 1%, no Zn–C bond peak was observed, whereas the intensity of this peak increased significantly when the C doping concentration was increased to 5%. This trend was also observed in the EDS and XPS results, which further confirmed that the C concentration of the doped material synthesized using the microwave method (3.74% by weight) was significantly higher than that of the material synthesized using the hydrothermal method (3.24% by weight). Doping ZnO with C increases the concentration of lattice defects and causes crystal stress, thereby forming Zn–O_{vac} bonds, which are observed in the O 1s XPS spectrum. O_{vac} is known to be involved in narrowing the band gap and is considered an electron "trapping" agent, which helps to separate photogenerated electron–hole pairs, thus enhancing the catalytic efficiency under visible light.

The XPS spectrum of the Ce 3d region is shown in Fig. 5G. The peaks at 881.68, 884.78, 897.88, and 900.02 eV are characteristic of the Ce $3d_{5/2}$ spin-orbitals, while the peaks at 903.48, 907.38, and 916.16 eV are characteristic of the Ce $3d_{3/2}$ spin-orbitals. The peaks related to the oxidation state of Ce^{4+} are obvious, including 881.68, 897.88, 900.7, 907.38, and 916.16 eV, while the weak peaks related to the oxidation state of Ce^{3+} include 884.78 and 903.31 eV.[28,64] ZnO dopes Ce, allowing it to exist in both Ce^{4+} and Ce^{3+} states, with Ce^{4+} being the predominant state. The Ce^{4+}/Ce^{3+} redox couple in the sample can capture electrons, which reduces the chances of electron–

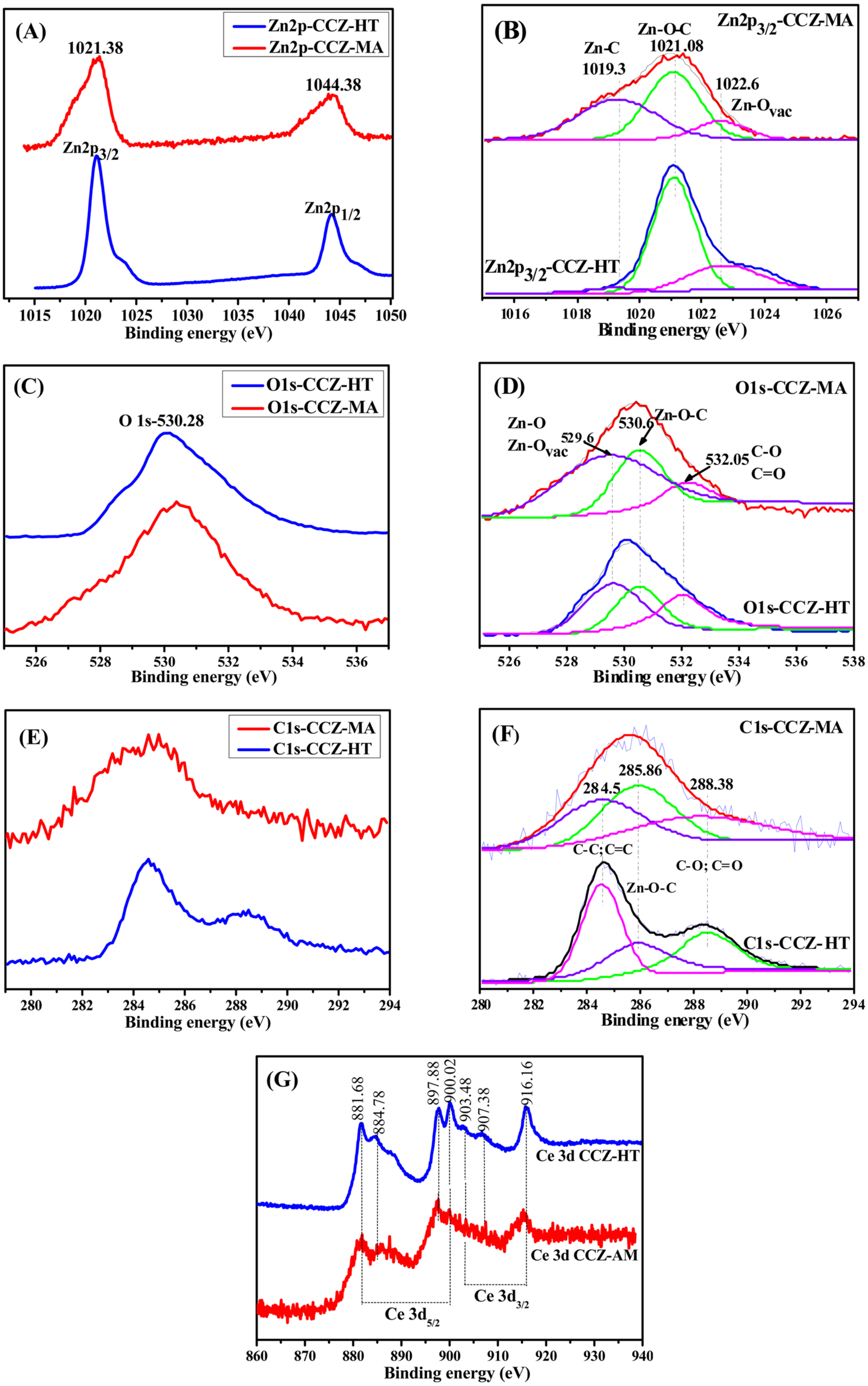

Fig. 5 Core-level XPS spectra of Zn 2p (A and E), O 1s (B and F), C 1s (C and G), and Ce 3d (D) of CCZ-HT and CCZ-MA samples.

hole pairs recombining. Furthermore, Ce^{3+} ions can interact with oxygen to produce ${}^{\bullet}O_2^-$ radicals (eqn (2) and (3)), thereafter engaging in a sequence of intermediate events that yield ${}^{\bullet}OH$ radicals, so enhancing the efficiency of the photocatalytic activity.

$$Ce^{4+} + e^- \rightarrow Ce^{3+} \tag{2}$$

$$Ce^{3+} + O_2 \rightarrow {}^{\bullet}O_2^- + Ce^{4+} \tag{3}$$

3.2. Photocatalytic decomposition of Ofx

Fig. 6A illustrates the breakdown of Ofx by the catalysts under visible light at natural pH. The findings demonstrated that Ofx diminished over time owing to the effects of the catalyst and light, following the sequence ZnO < Ce-ZnO < CCZ-HT < CCZ-MA. The kinetics of the photodegradation of the catalysts were assessed by analyzing the relationship between $\ln(C_0/C_t)$ and the reaction time. The correlation coefficients R^2 for the reactions were approximately 1, indicating that the degradation kinetics of the photodegradation of Ofx were accurately modelled using pseudo-first-order kinetics. The reaction rate constants k_{app} (Fig. 6B) for the ZnO, Ce-ZnO, CCZ-HT, and CCZ-MA catalysts were 0.0057, 0.0110, 0.0150, and 0.0193 min^{-1}, respectively. Analysis of the Kapp values revealed that CCZ-HT and CCZ-MA degraded Ofx more rapidly than the Ce-ZnO catalyst and significantly faster than ZnO. CCZ-HT and CCZ-MA degraded Ofx 2.63 and 3.38 times more rapidly than ZnO, respectively.

The concurrent doping of C and Ce enhanced the photocatalytic activity of ZnO. This benefit resulted from enhanced photoabsorption characteristics of the material in the visible light spectrum and an increase in lattice defects attributed to C and Ce doping. The UV-vis-DRS results indicate that the visible light absorption capacity of CCZ-HT and CCZ-MA materials surpassed that of pure ZnO. The optical absorption wavelengths of CCZ-HT and CCZ-MA were $\lambda < 424$ nm and $\lambda < 435$ nm, respectively, whereas those of ZnO-TN and microwave ZnO were $\lambda < 413$ nm and $\lambda < 400$ nm, respectively. The recombination rate of photogenerated electron–hole pairs in CCZ-HT and CCZ-MA was markedly decreased in comparison to that of pure ZnO. The reduction in recombination rate is associated with the concentration of oxygen vacancies, which function as electron "traps" and promote the effective separation of photogenerated electrons and holes. The PL results indicate that the concentration of oxygen vacancies in C- and Ce-co-doped ZnO materials significantly exceeds that of pure ZnO. Moreover, in a comparative analysis of the photodegradation efficacy of Ofx, the degradation rate of Ofx in the CCZ-MA sample surpassed that of the CCZ-HT sample. This outcome indicates that CCZ-MA possesses multiple advantages over CCZ-HT, such as

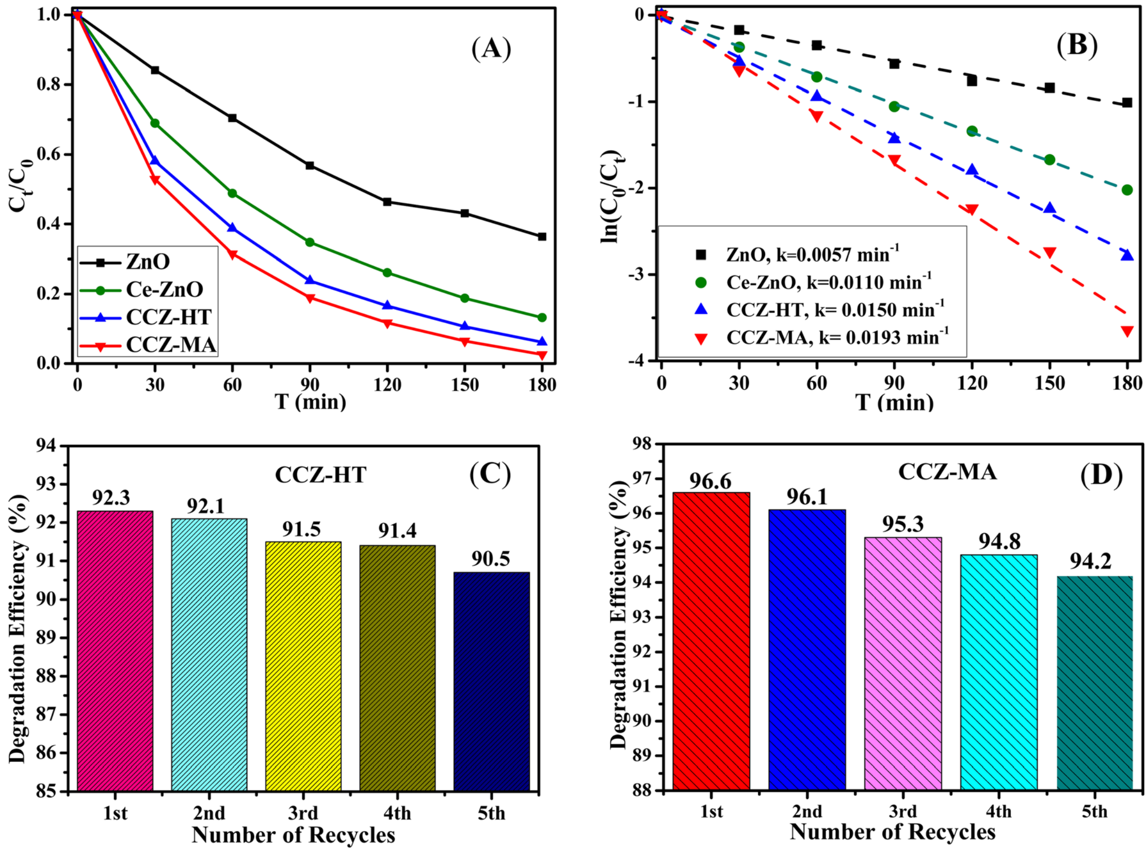

Fig. 6 (A) Ofx decomposition over time, (B) Pseudo-first-order kinetic plots of the Ofx photodegradation reaction, and (C and D) durability and recyclability test of the CCZ-HT and CCZ-MA over 5 cycles of OFL photodegradation under visible light.

a reduced band gap, increased oxygen vacancies, an expanded surface area, and enhanced charge separation. The narrow band gap is advantageous for the absorption of visible light. The extensive specific surface area enhances the adsorption of pollutants onto the catalyst surface. The heightened density of oxygen vacancy defects facilitates electron trapping, diminishes the recombination rate of photogenerated electron–hole pairs, and enhances the separation of photoinduced charge carriers.

In summary, the above analysis shows that microwave synthesis can rapidly produce CCZ-MA particles with more advantageous physicochemical and photocatalytic properties than CCZ-HT materials synthesised *via* the hydrothermal method.

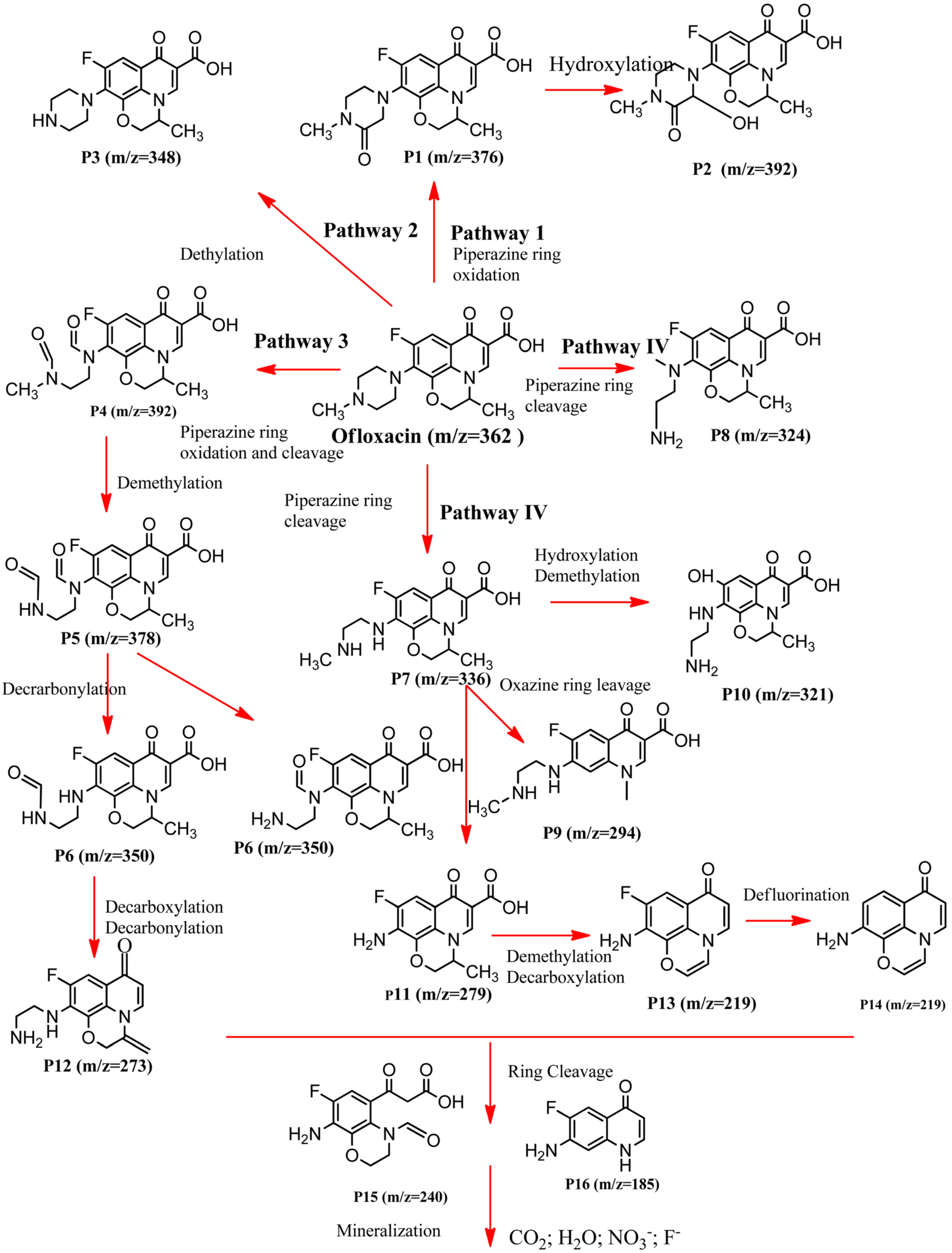

Fig. 7 Degradation pathways of Ofx using CCZ-MA under visible light.

The reusability of CCZ-HT and CCZ-MA materials for the photodegradation of OFx was evaluated after five cycles. Subsequent to each cycle, the materials were agitated in an aqueous solution, followed by filtration and multiple washings with distilled water and ethanol, before being dried at 80 °C for 10 hours. Fig. 6C and D illustrate the outcomes of the photodegradation of Ofx after five cycles. The results indicate that following each reuse, the photodegradation efficiency of Ofx diminished marginally, with a reduction of around 2% for the CCZ-HT catalyst and 2.5% for the CCZ-MA catalyst after five consecutive cycles. The CCZ-HT and CCZ-MA materials exhibit significant chemical and optical stability.

3.3. Ofx decomposition pathway and photocatalytic mechanism

The degradation products of Ofx were identified using the positive ion electrospray ionization mode (Fig. S1†), and the proposed degradation pathways are illustrated in Fig. 7.

Ofx was detected at $m/z = 362$.[65] The initial process involved the oxidation of the piperazine ring of Ofx, resulting in the derivative P1 ($m/z = 376$), which was hydroxylated to yield derivative P2 ($m/z = 392$).[66] The second pathway entailed the elimination of the methyl group from the piperazine ring, resulting in product P3 ($m/z = 348$).[67] In the third pathway, the piperazine ring in Ofx undergoes oxidation, followed by cleavage to yield P4 ($m/z = 392$) and demethylation to produce P5 ($m/z = 378$), culminating in the reduction of the carbonyl group to generate isomers of P6 ($m/z = 350$).[66] The fourth pathway involves the cleavage of the piperazine ring, resulting in products P7 ($m/z = 336$)[68] and P8 ($m/z = 324$).[65] The oxazine ring of product P7 is degraded at this stage, leading to the production of product P9 ($m/z = 294$).[69] The elimination of the hydroxyl, methyl, and methylamino groups from product P7 yielded products P10 ($m/z = 321$) and P11 ($m/z = 279$). The elimination of the carboxyl and methylamino groups from product P16 yielded P12 ($m/z = 273$).[69] The elimination of the carboxyl and methyl groups from the oxazine ring yields P13 (*m*/

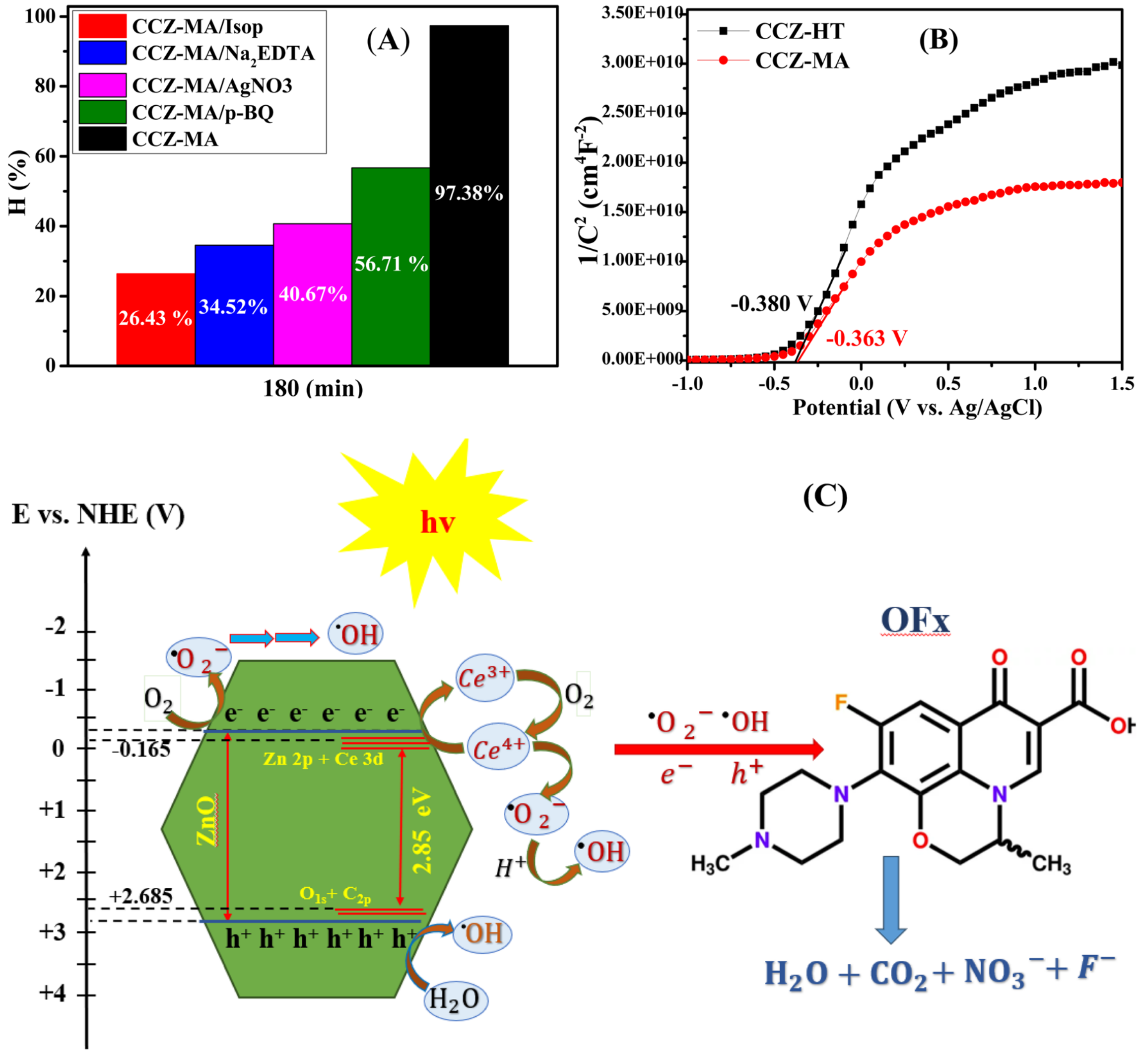

Fig. 8 (A) Effect of radical scavengers on Ofx degradation using CCZ-MA, (B) Mott–Schottky plot of CCZ-HT and CCZ-MA, and (C) hypothesized mechanisms for Ofx degradation using the CCZ-MA catalyst under visible light.

$z = 219$). The subsequent stage involves the elimination of the fluorine atom to yield P14 ($m/z = 201$). The reaction subsequently deconstructs the piperazine, oxazinyl, and carboxyl rings, resulting in the formation of the shorter-chain products P15 ($m/z = 240$) and P16 ($m/z = 185$).[70,71] The mineralization process yields CO_2, H_2O, NO_3^-, and NH_4^+.[66]

3.4. Mechanism

To elucidate the reaction process, studies were conducted to ascertain the role of reactive species in the photodegradation of Ofx using 1 mM selective scavengers. The tests used Na_2EDTA, *para*-benzoquinone (*p*-BQ), Isopropanol (Isop), and $AgNO_3$ to capture the reactive species hydrogen ions (h^+), superoxide radicals ($^{\bullet}O_2^-$), hydroxyl radicals ($^{\bullet}OH$), and electrons (e^-), respectively. The results in Fig. 8A illustrate a reduction in the degradation efficiency of Ofx after 180 min of illumination with the introduction of scavengers. The degradation efficiencies of Ofx were 26.43%, 34.52%, 40.67%, and 56.71% with the incorporation of Isop, Na_2EDTA, $AgNO_3$, and *p*-BQ, respectively. Simultaneously, the degradation efficiency of Ofx was 97.38% in the absence of any scavenger. This result proves that the reactive species $^{\bullet}OH$, h^+, $^{\bullet}O_2^-$, and e^- work together to degrade Ofx when exposed to light. The contributions of the reactive species are ranked in the following order: $^{\bullet}OH$ is the most effective, followed by h^+, e^-, and finally $^{\bullet}O_2^-$.

The band energy of a material can be determined using UV-vis-DRS or Mott–Schottky measurements. The conduction and valence band energies were calculated using eqn (4) and (5), respectively:

$$E_{VB} = \chi - E^c + 0.5 \times E_g \tag{4}$$

$$E_{CB} = E_{VB} - E_g \tag{5}$$

where E^c is the free electron energy on the hydrogen electrode scale (4.5 eV), E_{CB} is the conduction band energy, E_{VB} is the valence band energy, E_g is the band gap energy of ZnO, and χ is the Mulliken electronegativity of ZnO (5.76 eV).

Based on the bandgap energies extracted from the Tauc plots above, the valence band (E_{VB}) and conduction band (E_{CB}) potentials of the ZnO, CCZ-HT, and CCZ-MA samples were calculated according to eqn (1) and (2), respectively. For ZnO ($E_g = 3.10$ eV), the E_{VB} and E_{CB} values were determined to be 2.81 and −0.29 eV, respectively. For CCZ-HT ($E_g = 2.92$ eV), the E_{VB} and E_{CB} values were 2.72 eV and −0.20 eV, respectively. Meanwhile, for CCZ-MA ($E_g = 2.85$ eV), the E_{VB} and E_{CB} were calculated to be 2.685 eV and −0.165 eV, respectively.

Alternatively, Mott–Schottky measurements (Fig. 8B) provided flat band potentials of −0.380 V (CCZ-HT) and −0.363 V (CCZ-MA) *vs.* Ag/AgCl, corresponding to −0.183 V (CCZ-HT) and −0.166 V (CCZ-MA) *vs.* NHE after conversion. Assuming n-type semiconductor behavior, the flat band potentials are close to the conduction band edges, and subsequent calculations using the bandgap values yielded E_{VB} positions of 2.737 V for CCZ-HT and 2.684 V for CCZ-MA, respectively. Although minor differences were observed between the two methods, both approaches confirmed that Ce and C co-doping slightly upshifted the conduction band while narrowing the bandgap, thereby enhancing visible-light absorption and facilitating redox reactions during photocatalysis. Furthermore, Mott–Schottky plots revealed additional information about the defect concentration. The slope of the $1/C^2$ *versus* potential plot is inversely proportional to carrier density. The lower slope observed for CCZ-MA compared to that of CCZ-HT indicates a higher carrier (electron) concentration, which is consistent with the higher density of oxygen vacancies and intrinsic defects introduced during rapid microwave-assisted synthesis. These defects act as shallow donors and enhance visible-light-induced charge separation, playing a crucial role in the photocatalytic performance.

The way reactive species work and the energy levels of the CCZ-MA band help explain how Ofx breaks down when exposed to light, as shown in Fig. 8C. When visible light strikes CCZ-MA, its valence band electrons gain energy and transition to the conduction band, leading to the creation of holes in the valence band (eqn (6)). The conduction band of CCZ-MA (−0.165 V *vs.* NHE) is more negative than the reduction potential of $O_2/^{\bullet}O_2^-$ (−0.046 V), allowing electrons to combine with O_2 to generate the superoxide radical $^{\bullet}O_2^-$ (eqn (7)). When visible light strikes CCZ-MA, its valence band electrons gain energy and transition to the conduction band, leading to the creation of holes in the valence band (eqn (6)). The conduction band of CCZ-MA (−0.165 V *vs.* NHE) is more negative than the reduction potential of $O_2/^{\bullet}O_2^-$ (−0.046 V), allowing electrons to combine with O_2 to generate the superoxide radical $^{\bullet}O_2^-$ (eqn (7)).[72,73] In the valence band, holes can interact with H_2O to generate hydroxyl radicals $^{\bullet}OH$ (eqn (8)), as the valence band potential of CCZ-MA (+2.685 V) exceeds that of $^{\bullet}OH/H_2O$ (1.77–2.59 V).[74,75] The presence of Ce^{4+} and Ce^{3+} ions in the CCZ sample, predominantly Ce^{4+} (as indicated by XPS), generates $^{\bullet}O_2^-$ radicals and subsequently elevates the $^{\bullet}OH$ concentration (eqn (3), and (9)–(11)). Both e^-, h^+, $^{\bullet}O_2^-$, and $^{\bullet}OH$ facilitate the degradation of Ofx, resulting in the formation of CO_2, H_2O, and other inorganic compounds. The big improvement in how well the CCZ samples break down Ofx, compared to pure ZnO, is due to the presence of Ce^{4+} and Ce^{3+} ions and more oxygen vacancies in the doped material, which are known to trap electrons effectively. These components produce a synergistic effect, promoting the separation of photoexcited electrons and holes, therefore augmenting the photocatalytic efficiency of ZnO. The CCZ-MA material showed better photocatalytic activity than CCZ-HT because it has a better shape, a larger surface area, and more defects.

$$\text{CCZ-MA} + hv \rightarrow \text{CCZ-MA}\ (e^- + h^+) \tag{6}$$

$$e^- + O_2 \rightarrow {}^{\bullet}O_2^- \tag{7}$$

$$h^+ + H_2O \rightarrow {}^{\bullet}OH + H^+ \tag{8}$$

$${}^{\bullet}O_2^- + H^+ \rightarrow HOO^{\bullet} \tag{9}$$

$$HOO^{\bullet} + Ce^{3+} + H^+ \rightarrow H_2O_2 + Ce^{4+} \tag{10}$$

$$H_2O_2 + Ce^{3+} \rightarrow {}^{\bullet}OH + OH^- + Ce^{4+} \tag{11}$$

$$e^-, h^+, {}^{\bullet}OH, \text{ and } {}^{\bullet}O_2^- + Ofx \rightarrow CO_2 + H_2O + NO_3^- + SO_4^{2-} + F^- \ldots \quad (12)$$

4. Conclusion

In this study, Ce and C co-doped ZnO photocatalysts were successfully synthesized *via* hydrothermal and microwave-assisted methods and evaluated for their structural, optical, and photocatalytic properties. Both doping and the synthesis route significantly influenced morphology, crystalline defect concentration, specific surface areas, and electronic structure of the materials. Hydrothermal synthesis produced uniform nanoellipsoids with moderate crystallinity and defect density, while microwave-assisted synthesis generated fused flake-like structures with enhanced oxygen vacancy concentration and narrowed bandgap. Comprehensive characterization, including XRD, FE-SEM, PL, UV-vis DRS, XPS, and Mott–Schottky analysis, confirmed that Ce and C co-doping effectively modified the band structure by slightly upshifting the conduction band and reducing the bandgap, thereby extending light absorption into the visible region and improving charge carrier separation. These modifications directly contributed to improved photocatalytic performance in the degradation of ofloxacin under visible light. Among all samples, CCZ-MA exhibited the highest photocatalytic activity, which was attributed to its favourable morphology, higher carrier density, specific surface areas, and enhanced defect-related charge trapping. This work highlights the synergistic effect of co-doping and synthesis approaches in tuning ZnO-based photocatalysts and provides a promising strategy for designing efficient, visible-light-active materials for environmental remediation applications.

Data availability

Data of this article, including origin data, are available at DOI: https://doi.org/10.6084/m9.figshare.29098025.

Author contributions

Thi Viet Ha Luu: conceptualization, software, methodology, and writing – original draft. Thi Lieu Nguyen: formal analysis, software. Thi My Hien Bach: investigation and resources. Nguyen Trung Dung: investigation, resources, and supervision. Nguyen Nhat Huy: investigation and data curation. Phuc Huu dang: writing – review and editing.

Conflicts of interest

The authors declare that they have no conflict of interest.

References

1 S. Akhter, M. A. Bhat, S. Ahmed, W. A. Siddiqi, S. Ahmad and H. Shrimal, *Water*, 2023, **15**(3), 527.
2 D. Liu, Y. Zhang, Q. Yang, Y. Li, J. Li and X. Liao, *Bioresour. Technol.*, 2023, **371**, 128611.
3 Y. Deng, A. Debognies, Q. Zhang, Z. Zhang, Z. Zhou, J. Zhang, L. Sun, T. Lu and H. Qian, *Aquat. Toxicol.*, 2022, **244**, 106084.
4 C. N. C. Hitam and A. A. Jalil, *J. Environ. Manage.*, 2020, **258**, 110050.
5 C. B. Ong, L. Y. Ng and A. W. Mohammad, *Renewable Sustainable Energy Rev.*, 2018, **81**, 536–551.
6 S. Shukla, S. K. Shukla, P. Singh, H. Pandey, A. Dikshit and A. C. Pandey, *Heliyon*, 2025, **11**(2), e41816.
7 F. d. J. Silerio-Vázquez, L. A. González-Burciaga, C. Antileo, C. M. Núñez-Núñez and J. B. Proal-Nájera, *J. Hazard. Mater. Adv.*, 2024, **16**, 100506.
8 M. Hasham Firooz, A. Naderi, M. Moradi and R. R. Kalantary, *Sci. Rep.*, 2024, **14**(1), 4954.
9 D. Van Thuan, T. B. H. Nguyen, T. H. Pham, J. Kim, T. T. Hien Chu, M. V. Nguyen, K. D. Nguyen, W. A. Al-onazi and M. S. Elshikh, *Chemosphere*, 2022, **308**, 136408.
10 S. Shokrolahi, M. Farhadian and N. Davari, *J. Appl. Res. Water Wastewater*, 2019, **12**, 150–155.
11 T. Zhang, J. Liu, F. Zhou, S. Zhou, J. Wu, D. Chen, Q. Xu and J. Lu, *ACS Appl. Nano Mater.*, 2020, **3**, 9200–9208.
12 N. T. Dung, L. M. Thu, U. T. D. Thuy, V. T. Thien, N. T. Thuy, N. T. C. Tien, K. Y. A. Lin and N. N. Huy, *Environ. Sci. Nano*, 2022, **9**, 3973–3991.
13 S. Chakrabarti and B. K. Dutta, *J. Hazard. Mater.*, 2004, **112**, 269–278.
14 K. M. Lee, C. W. Lai, K. S. Ngai and J. C. Juan, *Water Res.*, 2016, **88**, 428–448.
15 P. Pandey, R. Kurchania and F. Z. Haque, *Opt. Spectrosc.*, 2015, **119**, 666–671.
16 T. V. H. Luu, H. Y. X. Nguyen, Q. T. Nguyen, Q. B. Nguyen, T. H. C. Nguyen, N. C. Pham, X. D. Nguyen, T. K. Nguyen and N. N. Dao, *RSC Adv.*, 2024, **14**, 12954–12965.
17 R. Peter, A. Omerzu, I. Kavre Piltaver, R. Speranza, K. Salamon, M. Podlogar, K. Velican, M. Percic and M. Petravic, *Ceram. Int.*, 2023, **49**, 35229–35238.
18 P. Yang, Y. Zhao and H. Yang, *Ceram. Int.*, 2015, **41**, 2446–2452.
19 P. L. Meena, A. K. Surela, L. K. Chhachhia, J. Meena and R. Meena, *Nanoscale Adv.*, 2025, **7**, 1335–1352.
20 M. B. Agarwal, S. Ali, M. Mehrotra, M. K. Panday, N. Gupta and S. Agarwal, in *Journal of Physics: Conference Series, Institute of Physics*, 2023, vol. 2570.
21 Y. R. Sui, B. Yao, Z. Hua, G. Z. Xing, X. M. Huang, T. Yang, L. L. Gao, T. T. Zhao, H. L. Pan, H. Zhu, W. W. Liu and T. Wu, *J. Phys. D Appl. Phys.*, 2009, **42**, 065101.
22 Z. F. Wang, Y. H. Zhang, J. Mao and J. Z. Wang, *Adv. Mater. Res.*, 2013, **834–836**, 12–17.
23 A. Joy, M. R. Viswanathan, B. K. Vijayan, C. G. Silva, I. Basheer, S. Sugathan, P. A. Mohamed, A. Solaiappan and A. Shereef, *RSC Adv.*, 2024, **14**, 21655–21667.
24 V. Kumari, A. Mittal, J. Jindal, S. Yadav and N. Kumar, *Front. Mater. Sci.*, 2019, **13**(9), DOI: 10.1007/s11706-019-0453-4.
25 W. Yu, J. Zhang and T. Peng, *Appl. Catal., B*, 2016, **181**, 220–227.

26 M. Rezaei and A. Habibi-Yangjeh, *Mater. Lett.*, 2013, **110**, 53–56.

27 Y.-I. Jung, B.-Y. Noh, Y.-S. Lee, S.-H. Baek, J. H. Kim and I.-K. Park, *Nanoscale Res. Lett.*, 2012, **7**, 43.

28 Q. Shi, C. Wang, S. Li, Q. Wang, B. Zhang, W. Wang, J. Zhang and H. Zhu, *Nanoscale Res. Lett.*, 2014, **9**, 480.

29 J. Iqbal, X. Liu, H. Zhu, C. Pan, Y. Zhang, D. Yu and R. Yu, *J. Appl. Phys.*, 2009, **106**, 1–7.

30 X. Shen, J. Sun, G. Zhu, Z. Ji, Z. Chen and N. Li, *J. Mater. Sci.*, 2013, **48**, 2358–2364.

31 L. T. V. Ha, L. M. Dai, D. N. Nhiem and N. Van Cuong, *J. Electron. Mater.*, 2016, **45**, 4215–4220.

32 T. Viet, H. Luu, Y. Xuan and T. Nguyen, *RSC Adv.*, 2024, **14**, 12954–12965.

33 Q. Luo, L. S. Wang, H. Z. Guo, K. Q. Lin, Y. Chen, G. H. Yue and D. L. Peng, *Appl. Phys. A: Mater. Sci. Process.*, 2012, **108**(1), DOI: 10.1007/s00339-012-6883-9.

34 L. T. V. Ha, L. M. Dai, D. T. Lim, D. N. Nhiem and N. N. Pham, *J. Chin. Chem. Soc.*, 2020, **67**, 1631–1643.

35 T. Viet, H. Luu, B. Nguyen, N. Dao and D. Luu, *RSC Adv.*, 2021, **11**, 36078–36088.

36 J. Iqbal, X. Liu, H. Zhu, C. Pan, Y. Zhang, D. Yu and R. Yu, *J. Appl. Phys.*, 2009, **106**, 1–7.

37 C. Karunakaran, P. Gomathisankar and G. Manikandan, *Mater. Chem. Phys.*, 2010, **123**, 585–594.

38 N. Kannadasan, N. Shanmugam, S. Cholan, K. Sathishkumar, G. Viruthagiri and R. Poonguzhali, *Mater. Charact.*, 2014, **97**, 37–46.

39 T. V. H. Luu, N. T. M. Tho, T. T. T. Thuy, L. N. Thong, N. T. Dung and P. H. Dang, *J. Sol-Gel Sci. Technol.*, 2024, **110**, 204–220.

40 J. J. Beltrán, C. A. Barrero and A. Punnoose, *Phys. Chem. Chem. Phys.*, 2019, **21**, 8808–8819.

41 J. Wojnarowicz, T. Chudoba and W. Lojkowski, *Nanomaterials*, 2020, **10**(6), 1086.

42 G. N. Dar, A. Umar, S. A. Zaidi, A. A. Ibrahim, M. Abaker, S. Baskoutas and M. S. Al-Assiri, *Sens. Actuators, B*, 2012, **173**, 72–78.

43 A. H. Wazir and I. W. Kundi, *J. Chem. Soc. Pak.*, 2016, **38**, 11–16.

44 S. Payrazm, S. Baghshahi, Z. Sadeghian and A. Aliabadizadeh, *Iran. J. Mater. Sci. Eng.*, 2022, **19**, 1–13.

45 M. E. Fleet, *Biomaterials*, 2009, **30**, 1473–1481.

46 S. Veerasingam and R. Venkatachalapathy, *Infrared Phys. Technol.*, 2014, **66**, 136–140.

47 D. Yang, Y. Li, Z. Tong, Y. Sun and Z. Jiang, *Ind. Eng. Chem. Res.*, 2014, **53**, 19249–19256.

48 A. S. Alshammari, L. Chi, X. Chen, A. Bagabas, D. Kramer, A. Alromaeh and Z. Jiang, *RSC Adv.*, 2015, **5**, 27690–27698.

49 L. Jia, C. Wu, S. Han, N. Yao, Y. Li, Z. Li, B. Chi, J. Pu and L. Jian, *J. Alloys Compd.*, 2011, **509**, 6067–6071.

50 R. Bomila, S. Srinivasan, A. Venkatesan, B. Bharath and K. Perinbam, *Mater. Res. Innovations*, 2018, **22**, 379–386.

51 K. Yi, H. Jiang, Y. Cai, G. Wang, F. Liu and D. Wang, *J. Univ. Sci. Technol. China*, 2024, **54**, 1–10.

52 M. Koyano, P. QuocBao, L. thi ThanhBinh, L. HongHa, N. NgocLong and I. Katayama, *Phys. Status Solidi A*, 2002, **193**(1), 125–131.

53 R. K. Biroju and P. K. Giri, *J. Appl. Phys.*, 2017, **122**(4), DOI: 10.1063/1.4995957.

54 A. S. Al-Fatesh, A. A. Ibrahim, A. H. Fakeeha, A. I. Osman, Y. M. Alanazi, F. S. Almubaddel and A. E. Abasaeed, *Nanomaterials*, 2024, **14**(15), 1320.

55 M. Thommes, K. Kaneko, A. V. Neimark, J. P. Olivier, F. Rodriguez-Reinoso, J. Rouquerol and K. S. W. Sing, *Pure Appl. Chem.*, 2015, **87**, 1051–1069.

56 X. Leng, S. Wei, Z. Jiang, J. Lian, G. Wang and Q. Jiang, *Sci. Rep.*, 2015, **5**, 1–11.

57 M. M. Liu, S. Y. Ma, Y. H. Cai, N. N. Ma, L. Wang and H. Sheng, *Ceram. Int.*, 2022, **48**, 22346–22353.

58 A. Alshammari, L. Chi, X. Chen, A. Bagabas, D. Kramer and A. Alromaeh, *RSC Adv.*, 2015, **5**, 27690–27698.

59 T. V. H. Luu, N. T. M. Tho, T. T. T. Thuy, L. N. Thong, N. T. Dung and P. H. Dang, *J. Sol-Gel Sci. Technol.*, 2024, **110**, 204–220.

60 G. R. Dillip, A. N. Banerjee, V. C. Anitha, B. Deva Prasad Raju, S. W. Joo and B. K. Min, *ACS Appl. Mater. Interfaces*, 2016, **8**, 5025–5039.

61 A. S. Alshammari, L. Chi, X. Chen, A. Bagabas, D. Kramer, A. Alromaeh and Z. Jiang, *RSC Adv.*, 2015, **5**, 27690–27698.

62 P. L. Meena, A. K. Surela, L. K. Chhachhia, J. Meena and R. Meena, *Nanoscale Adv.*, 2025, **7**, 1335–1352.

63 J. J. Beltrán, C. A. Barrero and A. Punnoose, *Phys. Chem. Chem. Phys.*, 2019, **21**, 8808–8819.

64 N. Kannadasan, N. Shanmugam, S. Cholan, K. Sathishkumar, G. Viruthagiri and R. Poonguzhali, *Mater. Charact.*, 2014, **97**, 37–46.

65 N. K. Joseph, V. J. Koshy, U. K. Aravind and C. T. Aravindakumar, *Chemosphere*, 2024, **361**, 142484.

66 R. Chen, S. Ding, N. Fu and X. Ren, *J. Environ. Chem. Eng.*, 2023, **11**, 109440.

67 W. Li, Y. Wu, Y. Gao and S. Xing, *Res. Chem. Intermed.*, 2019, **45**, 5549–5558.

68 Q. Shang, X. Liu, M. Zhang, P. Zhang, Y. Ling, G. Cui, W. Liu, X. Shi, J. Yue and B. Tang, *Chem. Eng. J.*, 2022, **443**, 136354.

69 P. Chen, Y. Gou, J. Ni, Y. Liang, B. Yang, F. Jia and S. Song, *Chem. Eng. J.*, 2020, **401**, 125978.

70 J. Tang, J. Xu, H. Zhang, W. Liu, H. Li, J. Xia and X. Xing, *Chem. Eng. J.*, 2023, **475**, 146023.

71 L. Zhang, Z. Cheng, X. Zhang, P. Chen, S. Tan and F. Qiu, *J. Water Proc. Eng.*, 2024, **59**, 105103.

72 W. Gu and Z. E. Peng, *Micro Nano Lett.*, 2020, **15**, 688–692.

73 Y. Fu, T. Huang, L. Zhang, J. Zhu and X. Wang, *Nanoscale*, 2015, **7**, 13723–13733.

74 W. H. Koppenol, D. M. Stanbury and P. L. Bounds, *Free Radicals Biol. Med.*, 2010, **49**(3), 317–322.

75 W. H. Koppenol and J. F. Liebman, *J. Phys. Chem.*, 1984, **88**, 99–101.